Proceedings of the ASME 2015 Pressure Vessels & Piping Conference
PVP2015
July 19-23, 2015, Boston, Massachusetts USA

PVP2015-45588

HIGH FIDELITY SIMULATION OF SAFETY RELIEF VALVE INTERNAL FLOWS

Yunchao Yang
Alexis Lefebvre
Ge-Cheng Zha *
Dept. of Mechanical and Aerospace Engineering
University of Miami
Coral Gables, Florida 33124
email: gzha@miami.edu

Qing-Feng Liu
Jun Fan
Dianjing Chen
Yuzhen Wu
National Engineering Research Center
for Special Pump and Valve
Beijing, 100176, China

ABSTRACT

This paper presents a numerical methodology and simulation for three-dimensional transonic flow in Safety Relief Valves. Simulation of safety relief valve flows is very challenging due to complex flow paths, high pressure variation, supersonic flow with shock and expansion waves, boundary layers, etc. The 3D unsteady Reynolds averaged Navier-Stokes (URANS) equations with one-equation Spalart-Allmaras turbulence model is used. A fifth order WENO scheme for the inviscid flux and a second order central differencing for the viscous terms are employed to discretize the Navier-Stokes equations. The low diffusion E-CUSP scheme used as the approximate Riemann solver suggested by Zha et al. is utilized with the WENO scheme to evaluate the inviscid fluxes. Implicit time marching method with 2nd order temporal accuracy using Gauss-Seidel line relaxation is employed to achieve a fast convergence rate. Parallel computing is implemented to save wall clock simulation time. The valve flows with air under different inlet pressures and temperatures are successfully simulated for the full geometry with all the fine leakage channels. A 3D mesh topology is generated for the complex geometry. Detailed simulations of air flow are accomplished with inlet gauge pressure 0.5MPa and 2.1MPa. The simulated air mass flow rate agrees excellently with the experimental results with an error of 0.26% for the inlet pressure of 0.5Mpa, and an error of 2.5% for the inlet pressure of 2.1MPa. The shock waves and expansion waves downstream of the orifice are very well resolved.

1 Introduction

Safety relief valves(SRV) are widely used in all pressure control systems such as power plants. Safety relief valves are designed to prevent overpressure by releasing excess fluid when the pressure reaches predetermined limit. A typical safety relief valve consists of a compression spring, which presses the valve spindle and disk on the valve seat to seal the pressurized system in the case of operating conditions below the valve set pressure. [1] Generally speaking, rapid opening and stable pressure release are desirable for a safety relief valve. Valve disc lift, blowdown and discharge depend on the internal flow structures generated within valve channels. However, transonic flow inside the valve is very complicated to understand due to its flow path with various sharp edges, small bumps and cavities, and high curvatures.

Also complex flow phenomena occur such as shock waves, expansions, and large separations. Both velocity measurement and flow visualization are difficult to perform within a commercial relief valve due to its complex geometry preventing effective use of invasive techniques to identify velocity profiles in the valve passages [2, 3].Thus computational fluid dynamics (CFD) becomes more and more popular in predicting the internal flow structures and their effects on discharge rate, flow forces and pressure field.
Vu and Wang [4] investigated the complex three-dimensional

*Address all correspondence to this author.

flow field of an oxygen safety pressure relieve valve with a CFD analysis, which provides a flow pattern that leads to the explanation of erosion pattern of hardware. Francis and Betts [2]investigated the incompressible flow structure within a valve using a commercial FEM software. Simulation results shows the flow field inside the valve and flow characteristics are identified with the transition between separated flow pattern. Morita et al. [5]studied the flow fluctuations around the steam control valve under the partial-opening condition, and conducted air experiments and CFD calculations to understand the cause of flow fluctuations. Dempster et al. [6, 7] conducted a two dimensional axisymmetric RANS approach with the k-ε turbulence model to predict the highly compressible flow, and studied the discharge flow rate, valve forces under different valve lift conditions using the commercial CFD software Fluent. Moncalvo et al. [8] studied the effect of grid fineness of the flow volume discretization and turbulence models on the accuracy of air mass flow using the CFD software ANSYS CFX-Flo. Bassi et al. [9] present a discontinuous Galerkin (DG) discretization of the compressible RANS and k-ω turbulence model equations for two-dimensional axisymmetric flows, compared the predicted flow capacity and pressure inside the bonnet against the experiment data. Beune et al. [1, 10] developed a multi-mesh numerical valve model to analyze the opening characteristic of high pressure safety valves with fluid-structural interaction, aiming to optimize the valve design based on the commercial software CFX. Song et al. [11, 12] investigated the dynamic flow characteristics of a direct-operated safety relief valve with moving mesh capabilities, multiple domains and valve piston motion using CFX. With a geometrically accurate CFD model of the SRV and the vessel, the complete transient process of the system from valve opening to valve closure was simulated.

The objective of this paper is to simulate the flow field of internal flow inside a safety relief valve with high fidelity CFD algorithms to better understand the transonic flow phenomena such as flow separation and reattachment, shock waves and supersonic expansion. The computed mass flow rates agree well with the experiment measured results.

2 Numerical Methods

The FASIP (Flow-Acoustics-Structure Interaction Package) CFD code is used to conduct the numerical simulation. The 3D Reynolds unsteady averaged Navier-Stokes (URANS) equations with one-equation Spalart-Allmaras [13] turbulence model is used. A 5th order WENO scheme for the inviscid flux [14–20] and a 2th order central differencing for the viscous terms [14, 19] are employed to discretize the Navier-Stokes equations. The low diffusion E-CUSP scheme used as the approximate Riemann solver suggested by Zha et al [15] is utilized with the WENO scheme to evaluate the inviscid fluxes. Implicit time marching method with 2nd order temporal accuracy using Gauss-Seidel line relaxation is employed to achieve a fast convergence rate [21]. Parallel computing is implemented to save wall clock simulation time [22].

2.1 Governing Equations

The Reynolds Averaged Navier Stokes (RANS) equations are solved with the Spalart-Allmarasone equation turbulence model (S-A) suggested by Spalat [13]. In generalized coordinate system, the conservative form of the equations are given as the following:

$$\frac{\partial Q}{\partial t}+\frac{\partial \mathbf{E}}{\partial \xi}+\frac{\partial \mathbf{F}}{\partial \eta}+\frac{\partial \mathbf{G}}{\partial \zeta}=\frac{1}{\mathrm{Re}}\left(\frac{\partial \mathbf{R}}{\partial \xi}+\frac{\partial \mathbf{S}}{\partial \eta}+\frac{\partial \mathbf{T}}{\partial \zeta}+\mathbf{D}\right) \tag{1}$$

The conservative variables **Q**, the inviscid flux **E**, the viscous flux **R**, and the source term are expressed as follows and the rest can be expressed following the symmetric rule.

$$\mathbf{Q}=\frac{1}{\mathrm{J}}\left[\rho,\, \rho u,\, \rho v,\, \rho w,\, \rho e,\, \rho\tilde{\nu}\right]^{T} \tag{2}$$

$$\mathbf{E}=\begin{bmatrix} \rho U \\ \rho u U+l_x p \\ \rho v U+l_y p \\ \rho w U+l_z p \\ (\rho e+p)U-l_t p \\ \rho\tilde{\nu}U \end{bmatrix} \tag{3}$$

$$\mathbf{R}=\begin{bmatrix} 0 \\ l_k\tau_{xk} \\ l_k\tau_{yk} \\ l_k\tau_{zk} \\ l_k(u_i\tau_{ki}-q_k) \\ \frac{\rho}{\sigma}(\nu+\tilde{\nu})(\mathbf{l}\bullet\nabla\tilde{\nu}) \end{bmatrix} \tag{4}$$

$$\mathbf{D}=\frac{1}{\mathrm{J}}\left[0,\, 0,\, 0,\, 0,\, 0,\, 0,\, S_{\nu}\right]^{T} \tag{5}$$

$$S_\nu = \rho C_{b1}(1-f_{t2})\tilde{S}\tilde{\nu} + \frac{1}{\mathrm{Re}}\left[-\rho\left(C_{w1}f_w - \frac{C_{b1}}{\kappa^2}f_{t2}\right)\left(\frac{\tilde{\nu}}{d}\right)^2 + \frac{\rho}{\sigma}C_{b2}(\nabla\tilde{\nu})^2 - \frac{1}{\sigma}(\nu+\tilde{\nu})\nabla\tilde{\nu}\bullet\nabla\rho\right] + \mathrm{Re}\left[\rho f_{t1}(\Delta U)^2\right] \quad (6)$$

In the equations above, U, V and W are the contravariant velocities in ξ, η and ζ directions.

$$\begin{aligned} U &= l_t + \mathbf{l}\bullet\mathbf{V} = l_t + l_x u + l_y v + l_z w \\ V &= m_t + \mathbf{m}\bullet\mathbf{V} = m_t + m_x u + m_y v + m_z w \\ W &= n_t + \mathbf{n}\bullet\mathbf{V} = n_t + n_x u + n_y v + n_z w \end{aligned} \quad (7)$$

The shear-stress τ_{ik} and total heat flux q_k in Cartesian Coordinate can be expressed as

$$\tau_{ik} = (\mu+\mu_t)\left[\left(\frac{\partial u_i}{\partial x_k} + \frac{\partial u_k}{\partial x_i}\right) - \frac{2}{3}\delta_{ik}\frac{\partial u_j}{\partial x_j}\right] \quad (8)$$

$$q_k = -\left(\frac{\mu}{\mathrm{Pr}} + \frac{\mu_t}{\mathrm{Pr}_t}\right)\frac{\partial T}{\partial x_k} \quad (9)$$

where, Pr is the Prandtl number, Pr_t is the turbulent Prandtl number, μ is the molecular viscosity determined by Sutherland law and μ_t is the turbulent viscosity determined by the S-A model [13]

2.2 The Low Diffusion E-CUSP (LDE) Scheme

The LDE flux vector splitting scheme suggested by Zha et al [15] is used to calculate the inviscid fluxes. The basic idea is to split the inviscid flux into the convective flux E^c and the pressure flux E^p. The flux vector $\mathbf{E}$ can be splitted as follows:

$$\mathbf{E} = E^c + E^p = \begin{pmatrix} \rho U \\ \rho u U \\ \rho v U \\ \rho w U \\ \rho e U \\ \rho\tilde{\nu} U \end{pmatrix} + \begin{pmatrix} 0 \\ l_x p \\ l_y p \\ l_z p \\ p\overline{U} \\ 0 \end{pmatrix} \quad (10)$$

The convective term, E^c is evaluated by

$$E^c = \rho U\left(1,\, u,\, v,\, w,\, e,\, \tilde{\nu},\right)^T = \rho U f^c \quad (11)$$

Let

$$C = c\left(l_x^2 + l_y^2 + l_z^2\right)^{\frac{1}{2}} \quad (12)$$

where $c = \sqrt{\gamma RT}$ is the speed of sound. Then the convective flux at interface $i+\frac{1}{2}$ is evaluated as:

$$E^c_{i+\frac{1}{2}} = C_{\frac{1}{2}}\left[\rho_L C^+ f^c_L + \rho_R C^- f^c_R\right] \quad (13)$$

where, the subscripts L and R represent the left and right hand sides of the interface.

The pressure flux, E^p is evaluated as the following

$$E^p_{i+\frac{1}{2}} = \begin{pmatrix} 0 \\ \mathcal{P}^+ p\, l_x \\ \mathcal{P}^+ p\, l_y \\ \mathcal{P}^+ p\, l_z \\ \frac{1}{2}p\left[\overline{U} + \overline{C}_{\frac{1}{2}}\right] \\ 0 \end{pmatrix}_L + \begin{pmatrix} 0 \\ \mathcal{P}^- p\, l_x \\ \mathcal{P}^- p\, l_y \\ \mathcal{P}^- p\, l_z \\ \frac{1}{2}p\left[\overline{U} - \overline{C}_{\frac{1}{2}}\right] \\ 0 \end{pmatrix}_R \quad (14)$$

2.3 The Fifth-Order WENO Scheme

The interface flux, $E_{i+\frac{1}{2}} = E(Q_L, Q_R)$, is evaluated by determining the conservative variables Q_L and Q_R using fifth-order finite difference WENO scheme [19] and [20]. For example,

$$(Q_L)_{i+\frac{1}{2}} = \omega_0 q_0 + \omega_1 q_1 + \omega_2 q_2, \quad (15)$$

where

$$\begin{aligned} q_0 &= \tfrac{1}{3}Q_{i-2} - \tfrac{7}{6}Q_{i-1} + \tfrac{11}{6}Q_i \\ q_1 &= -\tfrac{1}{6}Q_{i-1} + \tfrac{5}{6}Q_i + \tfrac{1}{3}Q_{i+1} \\ q_2 &= \tfrac{1}{3}Q_i + \tfrac{5}{6}Q_{i+1} - \tfrac{1}{6}Q_{i+2} \end{aligned} \quad (16)$$

The viscous terms are discretized by a fully conservative second-order accurate finite central differencing scheme.

2.4 Implicit Time Integration

The time dependent governing equations are solved using dual time stepping method suggested by [23]. To achieve high convergence rate, the implicit pseudo time marching scheme is used with the unfactored Gauss-Seidel line relaxation.

The physical temporal term is discretized implicitly using a three point, backward differencing as the following:

$$\frac{\partial Q}{\partial t} = \frac{3Q^{n+1} - 4Q^n + Q^{n-1}}{2\Delta t}, \tag{17}$$

where $n-1$, n and $n+1$ are three sequential time levels, which have a time interval of Δt. The first-order Euler scheme is used to discretize the pseudo temporal term. The semi-discretized equations of the governing equations are finally given as the following:

$$\begin{aligned}&\left[\left(\tfrac{1}{\Delta\tau} + \tfrac{1.5}{\Delta t}\right) I - \left(\frac{\partial R}{\partial Q}\right)^{n+1,m}\right] \delta Q^{n+1,m+1} \\ &= R^{n+1,m} - \tfrac{3Q^{n+1,m} - 4Q^n + Q^{n-1}}{2\Delta t},\end{aligned} \tag{18}$$

where the $\Delta\tau$ is the pseudo time step, R is the net flux evaluated on a grid point using the fifth-order finite difference WENO scheme for the inviscid fluxes and the fourth-order central differencing scheme for the viscous terms [17, 19, 20].Thirty pseudo time steps are used within each physical time step.

Figure 1: Safety relief valve investigated

3 Simulation Case Settings

The simulations are conducted for the safety relief valve, designed by National Engineering Research Center for Special Pump and Valve in China. In Fig. 1, The full geometry includes all the fine leakage channels, the gear teeth, the very small seal block, and the cavity around the valve. The boundary conditions and mesh used in the simulation are discribed below.

Two cases are simulated. The first case has lower inlet pressure and temperature and the second case has higher values. In the first case, the tiny leakages above valve disc is neglected during simulation to achieve the basic understanding of the flow field. . In the second full geometry case, all geometry details above the valve disc are simulated.

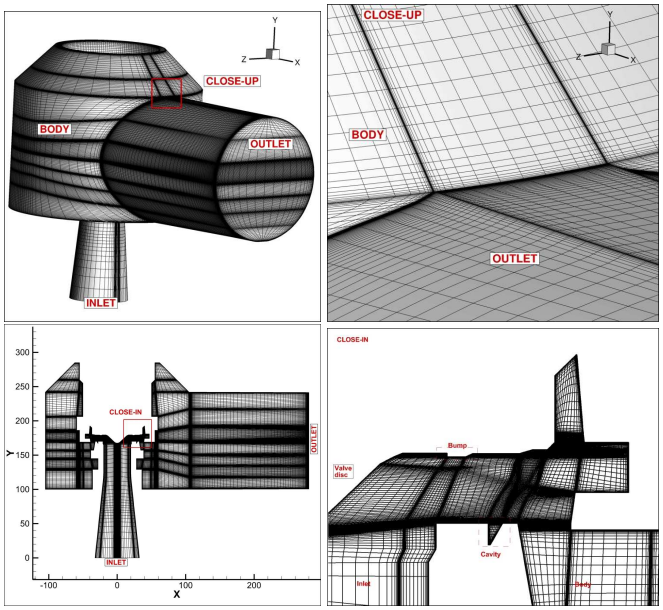

Figure 2: Mesh for the slightly modified valve geometry for low pressure air flow simulation

3.1 Boundary Conditions and Mesh

Total pressure, total temperature and flow angles are specified as the inlet boundary and static pressure is specified at the outlet boundary as shown in Table 3.1. The mesh without the tiny leakages is shown in Fig. 2, which is used in the first case. For the full geometry case, the mesh details is shown in Fig. 8. The no-slip boundary condition is applied at walls.

Table 1: Geometry and mesh in simulation

case	Mesh size(cells)	leakage	fluid
1	10,368,000	no	air
2	14,049,000	yes	air

Table 2: Simulation case descriptions

case	P_t inlet	T_t inlet	P_s outlet
1	0.5 MPa	272.16 K	0.1 MPa
2	2.1 MPa	301.8 K	0.1 MPa

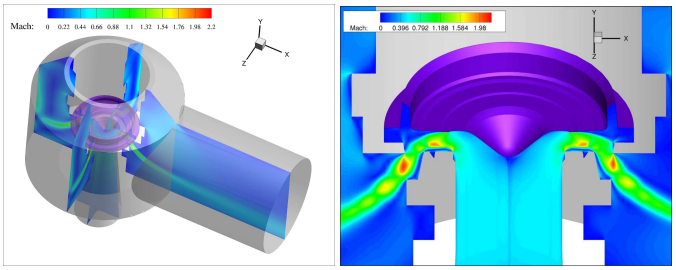

Figure 3: Mach number contours for the flow inside the valve body and close-up of the valve tunnel for low pressure air flow simulation

4 Results and Discussion

The comparison of simulation results with experiments are shown in Table 3. Mass flow simulations with low and high pressures predict excellent agreement with the measured results in the experiment. All the errors for air flow are lower than 2.5% and in the same order of the mass flow measurement uncertainty.

Table 3: Mass flow rate comparison between the simulation and experiment

case	1	2
P_t	0.5 MPa	2.1 MPa
$\dot{m}_{Exp.}$	1.54 Kg/s	5.07Kg/s
$\dot{m}_{Cal.}$	1.544 Kg/s	4.95Kg/s
Error	0.26%	-2.5%

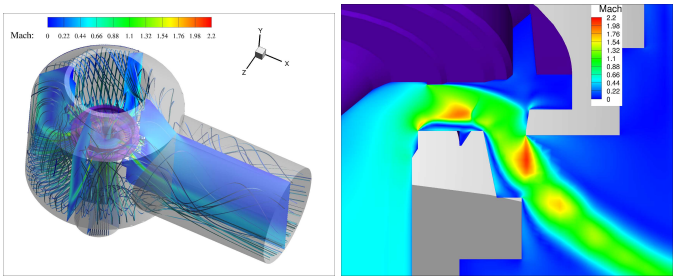

Figure 4: Mach number contours for the flow inside the valve body with streamlines and close-up of the valve tunnel for low pressure air flow simulation

4.1 Low pressure air flow without tiny leakage channels

The simulated Mach number contours across crosssection of the valve are shown in Fig. 3. Air flow speed reaches supersonic with the maximum Mach number of 2.2 at the valve opening with a near 180° flow U turn. A strong shock wave appears at the flow turning. The flow is choked in the orifice area located at the beginning and the end of the U turn. After the orifice section the flow becomes supersonic again.

The streamlines through the flow path inside the valve are displayed on the left of Fig. 4. Due to the valve inner geometries with bumps and cavities, vortexes and shock waves are generated. . The flow exits from the valve cover, forms a vortex in the circumference of the valve body and generates two counter-rotating vortex tubes in the outlet pipe. The right of Fig. 4 shows U turn flow field inside the valve.

Detailed inner flow structures are displayed in Fig. 5 at different locations. The top left figure of Fig. 5 shows that flow accelerates at the valve tunnel inlet, is choked, and becomes supersonic with several shockwaves and expansions occuring during flow pass valve tunnel. The top-right figures shows that flow gets choked in the bump region and reduces flow passing area. As the flow get into the valve, due to the effect of cavities, three vortex regions are generated as indicated in middle left figure of Fig. 5. At the inlet of valve tunnel, large separation appears due to sharp edge turn near 90 degree. At the outlet of valve tunnel, there is also a sharp turning with a strong shock wave and expansion waves.

Fig. 6 shows the total pressure contours. The U turning appears to be the main source of total pressure loss with a drop of total pressure about 50%.

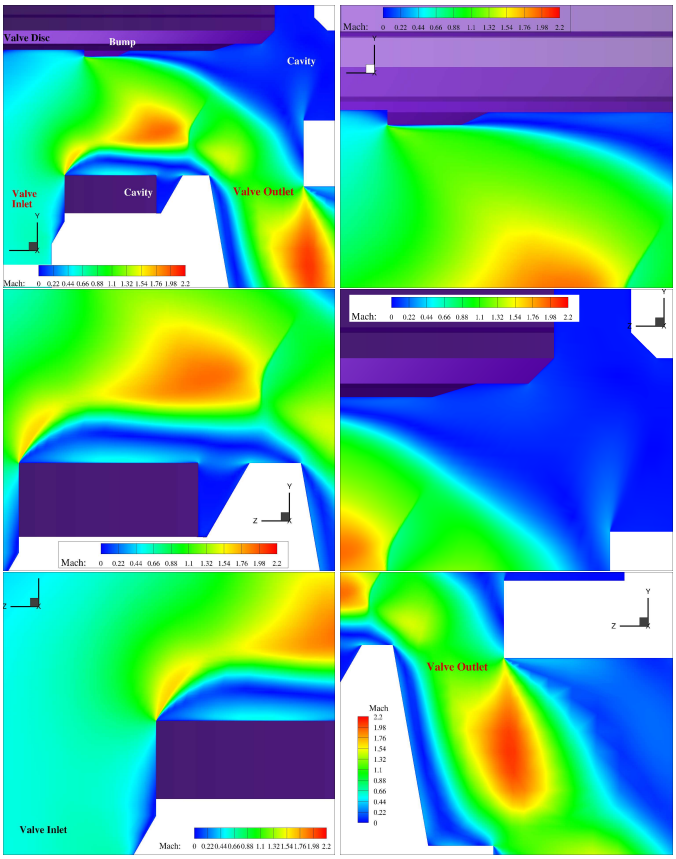

Figure 5: Detailed Mach number contour in the valve tunnel at different locations for low pressure air flow simulation

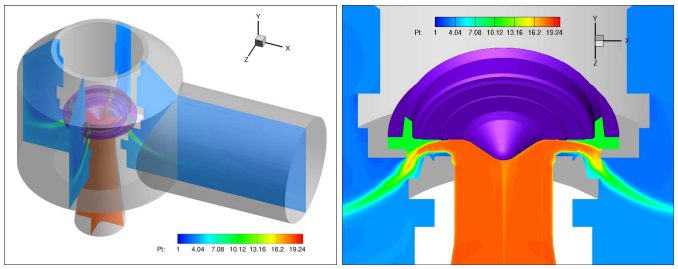

Figure 6: Total pressure contours for the flow inside the valve body and close-up of the valve tunnel for low pressure air flow simulation

The static pressure contours shown in Fig. 7 indicates that the highest pressure region is located on the valve disc near the top stagnation point. Static pressure drops rapidly when the flow passes the valve tunnel.

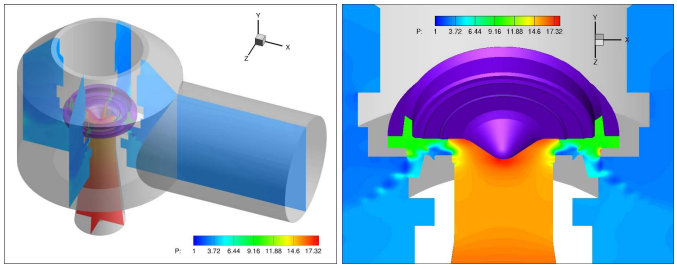

Figure 7: Static pressure contours for the flow inside the valve body and close-up of the valve tunnel for low pressure air flow simulation

4.2 High pressure air flow with tiny leakage channels

This case has a higher inlet pressure of 2.1MPa as indicated in Table 3.1. All fine leakage channels are with a total size of 15×10^6 grid points, as shown in Fig. 8. The high pressure air flow simulation predicts a mass flow of 4.95 kg/s, which is in excellent agreement with 5.07 kg/s measured in the experiment. The error is about -2.5%.

The high pressure air flow simulated Mach number contours are shown in Fig. 9,which shows the similar flow structures as the case with low inlet pressure in last section. Flow reaches supersonic with the maximum Mach number of 2.8 downstream of the outlet of the valve opening with a near 180° U-type flow turn. Similar to the low pressure simulation, air flow is also choked in the orifice located at the beginning and the end of the U turn. After valve orifice the flow becomes supersonic again like a Laval nozzle. Highest flow speed is identified at the exit of valve tunnel, which is delayed compared to low pressure flow. Streamlines in the whole flow domain are displayed in the left figure of Fig. 9. The flow filed and vortexes generated are displayed in right figure of Fig. 9.

Under higher pressure, stronger vortexes and strong shock waves are generated. The first figure of Fig. 10 shows the whole flow field inside the valve. The right figure in Fig. 10 shows the flow velocities get choked at the bump region, which result in a strong shock wave. At the inlet and outlet of valve U turning, there is a strong separation from the wall especially at the choke area, which blocks the flow area and restrain the mass flow rate. As the flow get in the valve, due to the effect of cavities, three vortex regions are generated as indicated in Fig. 10.

The flow exits from the valve cover and forms strong shock waves and vortexes in the circumference of the valve body and forms two counter-rotating vortex tubes in the outlet pipe. Fig.

10 also show the Mach number contours with velocity vector in the valve orifice region. There is a large separation when the flow turns right outside of the valve tunnel and a large separation is created as shown in the middle right figure of Fig. 10. Such separation will generate a large flow blockage and limit the mass flow rate.

Fig. 11 shows the total pressure contours. The U turn appears to be the main source of total pressure loss with a drop of $\approx 50\%$. The static pressure contours shown in Fig. 12 indicates that the highest pressure region is located in the valve cover surface due to the stagnation flow from the the flow turning. And pressure in the top part of leakage is also higher than outlet pressure, which produce lift force for the movement of valve.

Fig. 13 shows the velocity vector inside the top tiny leakage channels. It is observed that air flows downwards due to the pressure difference between the top cavity inside the valve and top pressure control chamber. Flow inside the small leakage is laminar flow because of the tiny circumferential leakage. The velocity of flow varies from zero at the walls to a maximum value along the center line of the channel. The velocity profile is the polynomial function of radius, which is the typical flow inside two infinitely large plates.

5 Conclusion

This paper has successfully developed a methodology for 3D unsteady compressible flow simulation of pressure valve flows. A 3D mesh topology with all the fine leakage channels is established for the complex geometry. Detailed simulations of air flow are accomplished with inlet gauge pressure 0.5 MPa and 2.1 MPa. The simulated air mass flow rate agrees excellently with the experimental results with an error of 0.26% for the inlet pressure of 0.5Mpa, and an error of 2.5% for the inlet pressure of 2.1MPa. The flow is observed to be choked at the valve opening with the flow U-turn location. The simulated results provide a good understanding of the flow field. It appears that this is the first time that a valve flow with fine leakage channels is successfully simulated using CFD. It can provide important design guidance to improve the valve flow capacity and dynamic performance.

6 Acknowledgement

This research is supported by the funding of National Engineering Research Center for Special Pump and Valve of China. The fourth author, Mr. Qing-Feng Liu, was sponsored by Chinese Scholar Council.

REFERENCES

[1] A. Beune, J. Kuerten, and J. Schmidt, "Numerical calculation and experimental validation of safety valve flows at pressures up to 600 bar," *AIChE Journal*, vol. 57, no. 12, pp. 3285–3298, 2011.

[2] J. Francis and P. Betts, "Modelling incompressible flow in a pressure relief valve," *Proceedings of the Institution of Mechanical Engineers, Part E: Journal of Process Mechanical Engineering*, vol. 211, no. 2, pp. 83–93, 1997.

[3] F. Bassi, A. Crivellini, V. Dossena, N. Franchina, and M. Savini, "Investigation of flow phenomena in air–water safety relief valves by means of a discontinuous galerkin solver," *Computers & Fluids*, vol. 90, pp. 57–64, 2014.

[4] B. Vu, T.-S. Wang, M.-H. Shih, and B. Soni, "Navier-stokes flow field analysis of compressible flow in a high pressure safety relief valve," *Applied mathematics and computation*, vol. 65, no. 1, pp. 345–353, 1994.

[5] R. Morita, F. Inada, M. Mori, K. Tezuka, and Y. Tsujimoto, "Cfd simulations and experiments of flow fluctuations around a steam control valve," *Journal of Fluids Engineering*, vol. 129, no. 1, pp. 48–54, 2007.

[6] W. Dempster, C. Lee, and J. Deans, "Prediction of the flow and force characteristics of safety relief valves," in *ASME 2006 Pressure Vessels and Piping/ICPVT-11 Conference*, pp. 93–99, American Society of Mechanical Engineers, 2006.

[7] W. Dempster and W. Elmayyah, "A computational fluid dynamics evaluation of a pneumatic safety relief valve," in *13th International Conference on Applied Mechanics and Mechanical Engineering (AMME-13)*, pp. 92–106, 2008.

[8] D. Moncalvo, L. Friedel, B. Jörgensen, and T. Höhne, "Sizing of safety valves using ansys cfx-flo®," *Chemical engineering & technology*, vol. 32, no. 2, pp. 247–251, 2009.

[9] F. Bassi, F. Cecchi, N. Franchina, S. Rebay, and M. Savini, "High-order discontinuous galerkin computation of axisymmetric transonic flows in safety relief valves," *Computers & fluids*, vol. 49, no. 1, pp. 203–213, 2011.

[10] A. Beune, J. Kuerten, and M. van Heumen, "Cfd analysis with fluid–structure interaction of opening high-pressure safety valves," *Computers & Fluids*, vol. 64, pp. 108–116, 2012.

[11] X. G. Song, L. Wang, and Y. C. Park, "Transient analysis of a spring-loaded pressure safety valve using computational fluid dynamics (cfd)," *Journal of Pressure Vessel Technology*, vol. 132, no. 5, p. 054501, 2010.

[12] X. Song, L. Cui, M. Cao, W. Cao, Y. Park, and W. M. Dempster, "A cfd analysis of the dynamics of a direct-operated safety relief valve mounted on a pressure vessel," *Energy Conversion and Management*, vol. 81, pp. 407–419, 2014.

[13] P. Spalart and S. Allmaras, "A One-equation Turbulence Model for Aerodynamic Flows." AIAA-92-0439, 1992.

[14] Y.-Q. Shen and G.-C. Zha, "Large Eddy Simulation Using a New Set of Sixth Order Schemes for Compressible Viscous Terms ," *Journal of Computational Physics*, vol. 229, pp. 8296–8312, 2010.

[15] G.-C. Zha, Y. Shen, and B. Wang, "An improved low diffusion E-CUSP upwind scheme ," *Journal of Computer & Fluids*, vol. 48, pp. 214–220, 2011.

[16] Y.-Q. Shen and G.-Z. Zha , "Generalized finite compact difference scheme for shock/complex flowfield interaction," *Journal of Computational Physics*, vol. doi:10.1016/j.jcp.2011.01.039, 2011.

[17] Shen, Y.-Q. and Zha, G.-C. and Wang, B.-Y., " Improvement of Stability and Accuracy of Implicit WENO Scheme," *AIAA Journal*, vol. 47, No. 2, pp. 331–344, 2009.

[18] Y.-Q. Shen, G.-C. Zha, and B.-Y. Wang, "Improvement of Stability and Accuracy of Implicit WENO Scheme ," *AIAA Journal*, vol. 47, pp. 331–344, 2009.

[19] Shen, Y.-Q. and Zha, G.-C. and Chen, X.-Y., " High Order Conservative Differencing for Viscous Terms and the Application to Vortex-Induced Vibration Flows," *Journal of Computational Physics*, vol. 228(2), pp. 8283–8300, 2009.

[20] Shen, Y.-Q. and Zha, G.-C. , " Improvement of the WENO Scheme Smoothness Estimator," *International Journal for Numerical Methods in Fluids*, vol. DOI:10.1002/fld.2186, 2009.

[21] G.-C. Zha and E. Bilgen, "Numerical Study of Three-Dimensional Transonic Flows Using Unfactored Upwind-Relaxation Sweeping Algorithm," *Journal of Computational Physics*, vol. 125, pp. 425–433, 1996.

[22] B.-Y. Wang and G.-C. Zha, "A General Sub-Domain Boundary Mapping Procedure For Structured Grid CFD Parallel Computation," *AIAA Journal of Aerospace Computing, Information, and Communication*, vol. 5, No.11, pp. 2084–2091, 2008.

[23] A. Jameson, "Time Dependent Calculations Using Multigrid with Application to Unsteady Flows past Airfoils and Wings." AIAA Paper 91-1596, 1991.

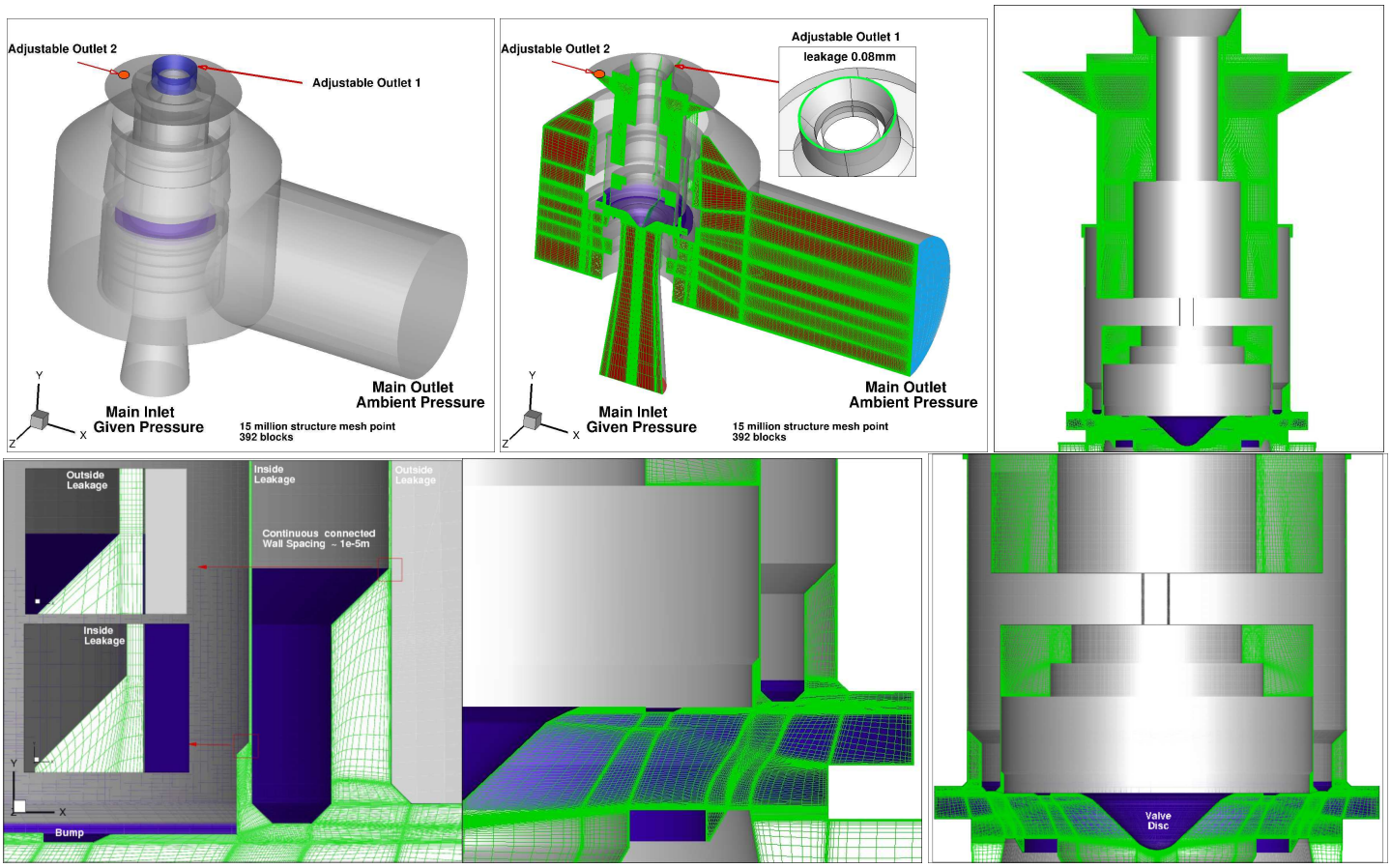

Figure 8: Mesh topology for the slightly modified valve geometry with top leakages for high pressure air flow simulation

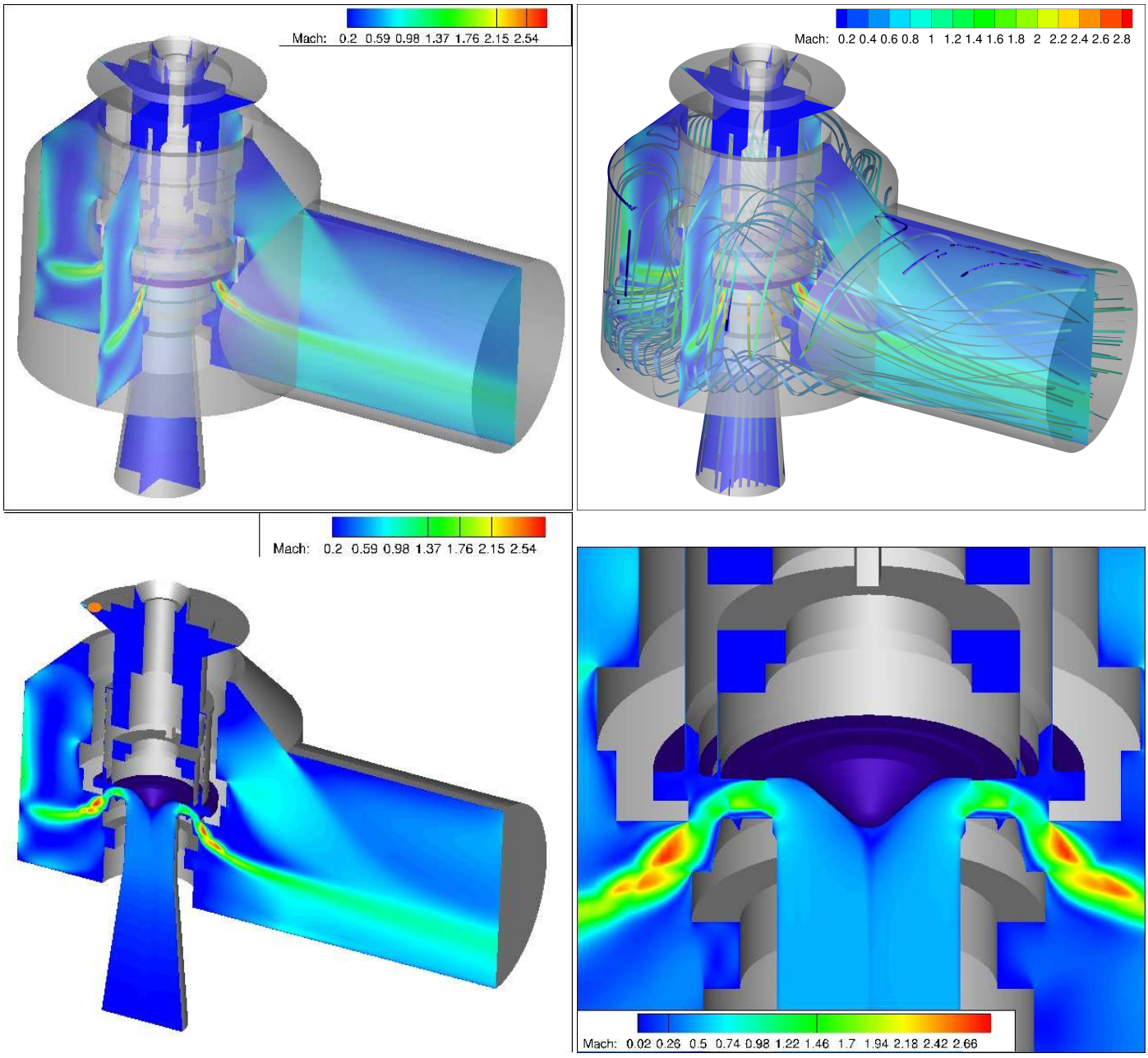

Figure 9: Mach number contours inside the valve with leakages for high pressure air flow simulation

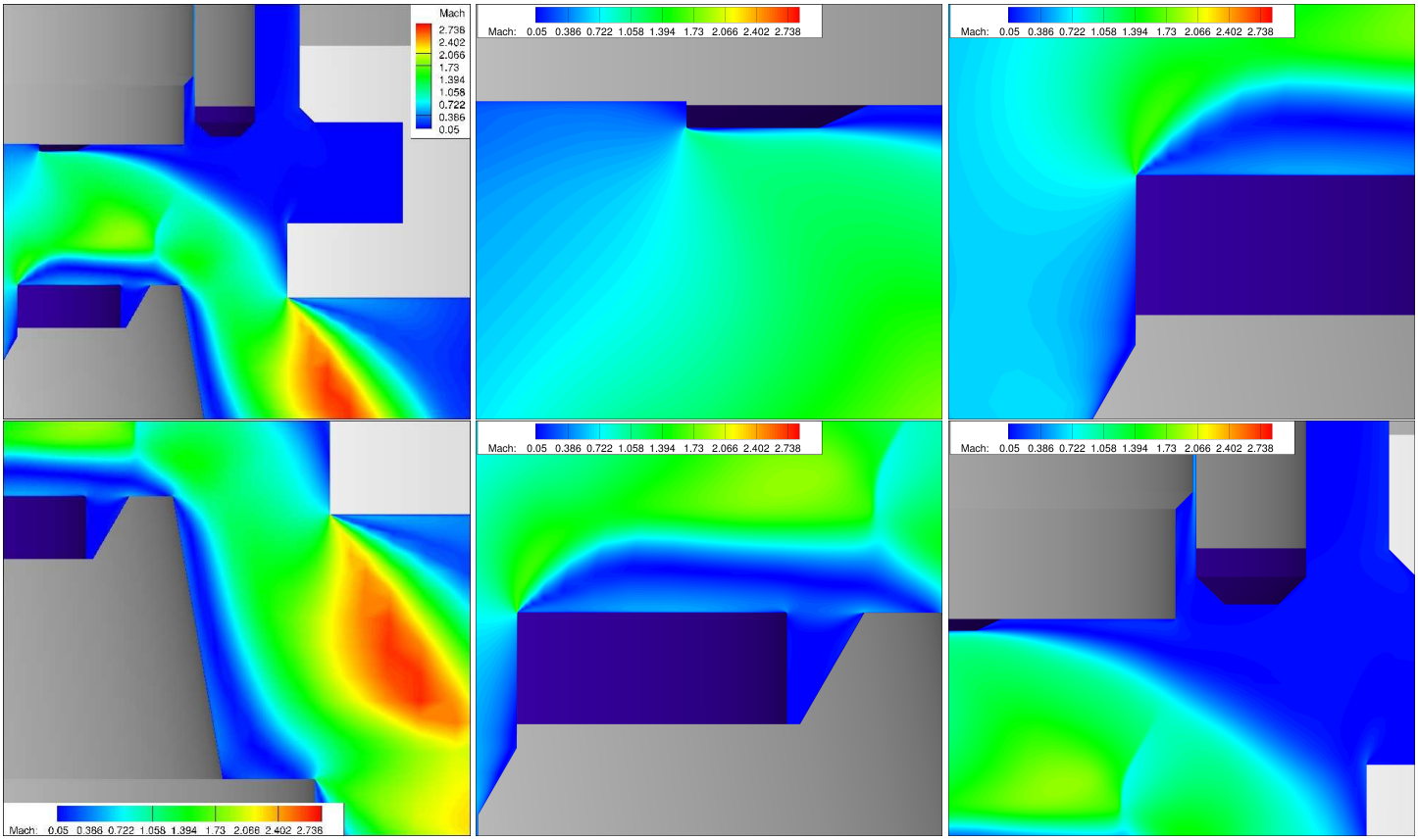

Figure 10: Detailed Mach number contours inside the valve tunnel with leakages for high pressure air flow simulation

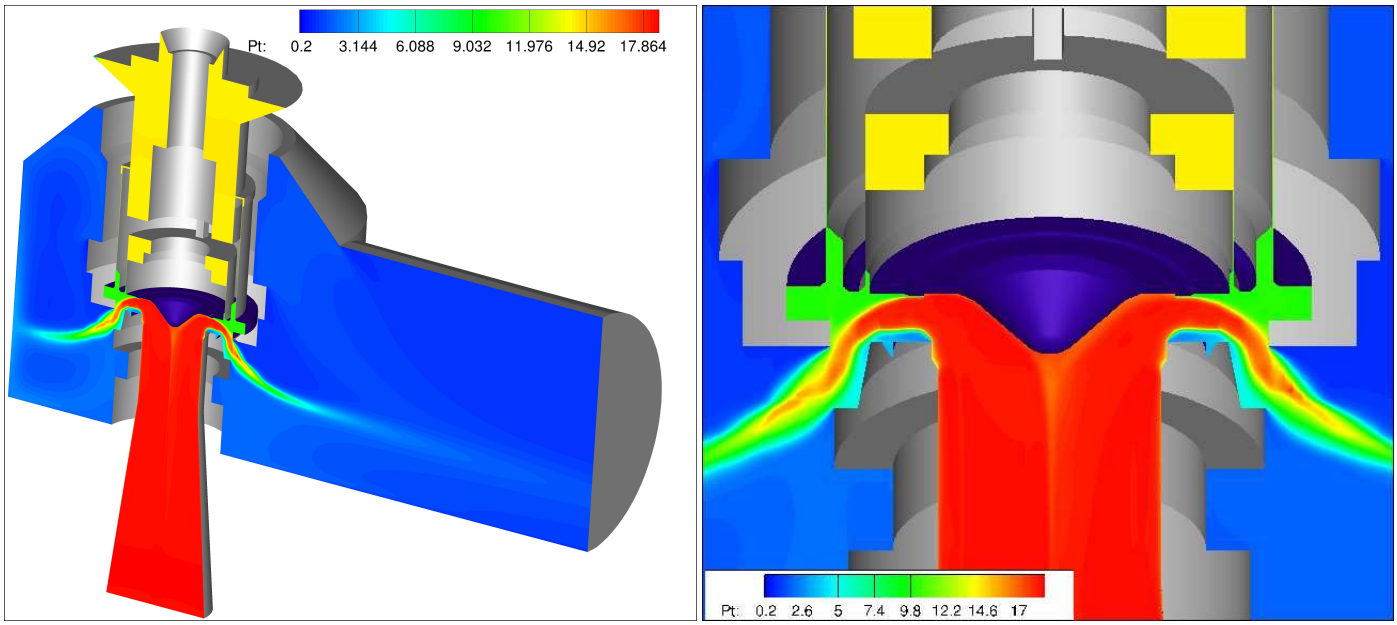

Figure 11: Total pressure contours for the flow inside the valve body with leakage for high pressure air flow simulation

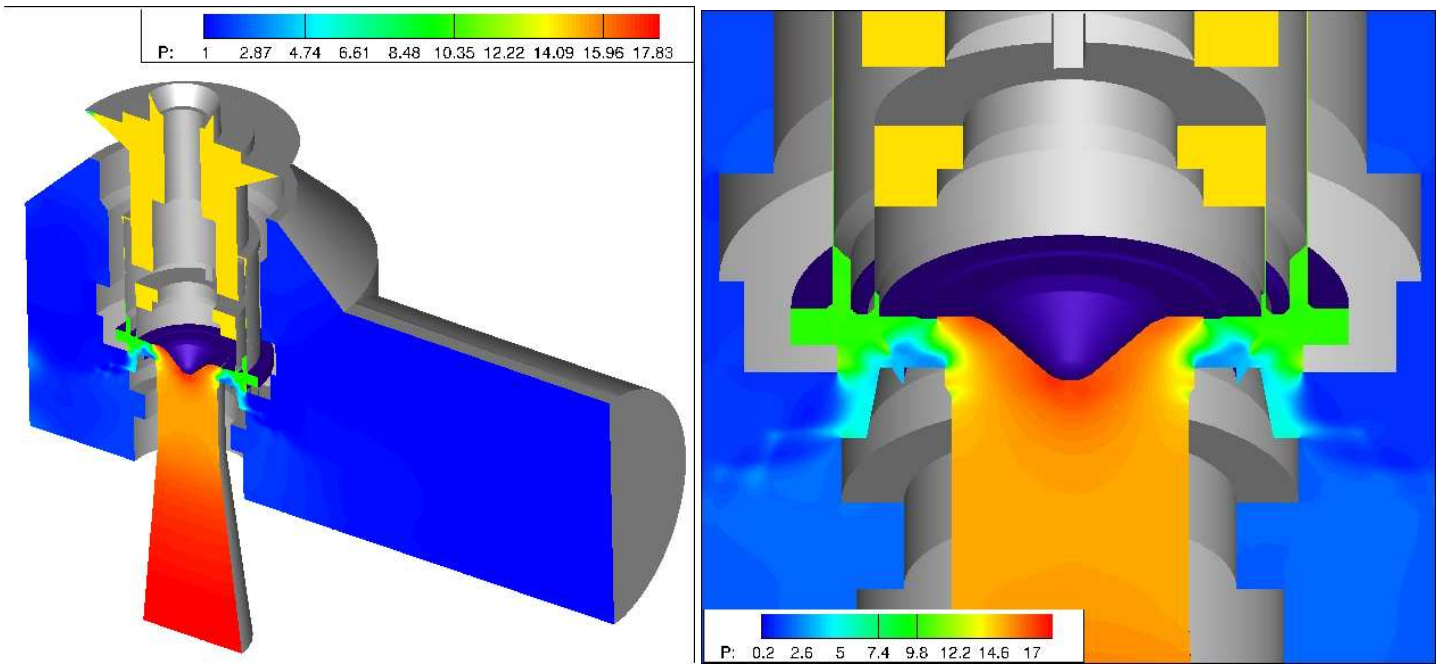

Figure 12: Static pressure contours for the flow inside the valve body with leakages for high pressure air flow simulation

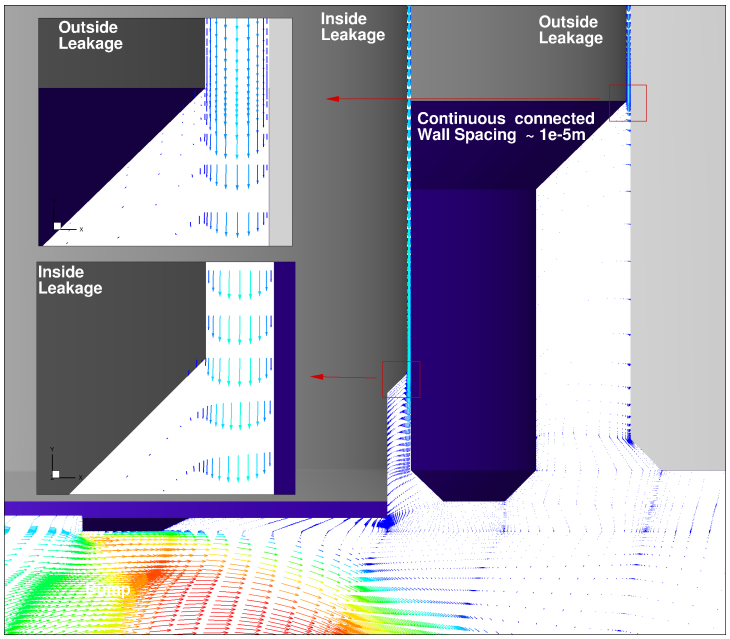

Figure 13: Detailed velocity vectors inside the tiny leakage channel for high pressure air flow simulation